SAND2018-2363J

# Lamb Wave Focusing Transducer for Efficient Coupling to Wavelength-Scale Structures in Thin Piezoelectric Films

Aleem Siddiqui, Roy H. Olsson III, and Matt Eichenfield

*Abstract*—**This article describes the theoretical and experimental investigation of interdigitated transducers (IDTs) capable of producing focused acoustical beams in thin film piezo-electric materials. A mathematical formalism describing focused acoustical beams, Lamb beams, is presented and related to their optical counterparts in two- and three-dimensions. A novel Fourier domain transducer design methodology was developed and utilized to produce near diffraction limited focused beams within a thin film AlN membrane. The properties of the acoustic beam formed by the transducer were studied by means of Doppler vibrometry implemented with a scanning confocal balanced homodyne interferometer. Fourier domain modal analysis confirmed that 85% of the acoustical power was delivered to the targeted focused beam which was constituted from the lowest order symmetric mode, while 2% was delivered unintentionally to the beam formed from the anti-symmetric mode, and the remaining power was isotropically scattered. The transmission properties of the acoustic beams as they interact with devices with wavelength scale features were also studied, demonstrating minimal insertion loss for devices in which a subwavelength, pinhole apertures was included.**

*Index Terms*—**Aluminum nitride; acoustic focusing; Lamb wave transducers, Doppler vibrometry**

## I. INTRODUCTION

IN recent years, the development of novel phononic and radio frequency (RF) devices has been enabled by topology miniaturization and material quality improvements in acoustic wavelength-scale structures. Surface acoustic wave (SAW) device performance has been pushed well into the GHz range and devices have been realized in compact, low-cost material platforms [1]–[3]. Phononic crystal waveguides and cavities have been demonstrated at both higher frequency and increasingly higher quality factor [4]–[7]. Additionally, nano-opto-mechanical devices exploiting strong phonon-photon interactions have led to quantum ground state cooling, phonon lasing and ultra-sensitive sensors and accelerometers [8]–[11]. These developments and others are expected to have a major impact on applications ranging from signal processing and RF communications, to acoustic imaging and nondestructive testing[12].

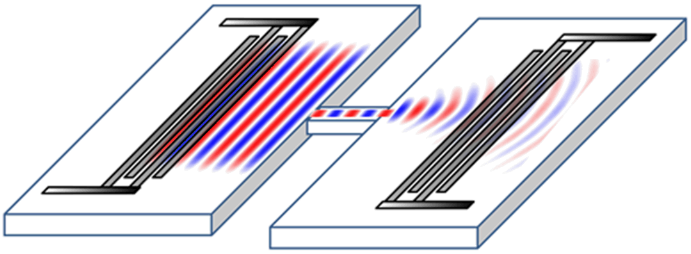

Figure 1. Illustration of the typical problem encountered with large transducers trying to excite wavelength-scale structures. The wave produced by the send transducer suffers an insertion loss at the waveguide input of approximately the ratio of the width of the waveguide to the width of the transducer. Intercepting the wave immediately at the waveguide output produces a second, symmetric insertion loss. If the transducer is offset from the waveguide output (as shown), diffraction expands the beam but causes wave front curvature that will tend to average the received signal to zero.

Emerging wavelength-scale devices resulting from this push toward higher frequency and improved functionality often require efficient excitation at the scale of a single wavelength. The size of practical RF piezo-electric transducers, however, is often constrained by RF impedance-matching requirements [13]. The electrical admittance of straight interdigital transducers (IDTs), for example, is characterized by a static total capacitance and a radiative conductance proportional to the total capacitance. Impedance matching is optimized through the radiative conductance via the static capacitance. In the gigahertz frequency regime, in particular, the IDT aperture must be kept sufficiently large to attain optimal matching to a 50Ω line, especially when matching networks are impractical. Straight IDTs thus have dimensions many wavelengths long and are therefore not compatible with a wavelength-scale excitation requirement. Thus, impedance matching considerations essentially guarantee that the power produced by a transducer will be spread over an area much larger than a wavelength and directly result in significant insertion loss on

---

Manuscript received. This work was supported by the Laboratory Directed Research and Development (LDRD) program at Sandia National Laboratories. Sandia National Laboratories is a multiprogram laboratory operated by the Sandia Corporation, Lockheed Martin Company, for the United States Department of Energy's National Nuclear Security Administration under contract DE-AC04-

A. Siddiqui is with the department of MEMS technologies at Sandia National Labs (e-mail: asiddq@sandia.gov).

R.H. Olson was formerly with the department of MEMS technologies at Sandia National Labs and is currently a DARPA program manager.

M. Eichenfield is with the department of MEMS technologies at Sandia National Labs (e-mail: asiddq@sandia.gov).

the send or receive transducer or both [14]. Fig. 1 illustrates this problem in a transmission configuration involving an acoustical waveguide.

Even if the transducer length was greatly reduced, mode mismatch due to diffraction would still lead to large insertion loss unless electrodes were directly deposited onto the waveguide, which from both a fabrication and impedance-matching perspective is impractical. The large number of electrodes in this case would also lead to excessively narrow filter bandwidths through increased filter-Q factors. IDTs with straight fingers, while optimized to produce straight crested Lamb waves, are ill-suited to serve as an electrical/phononic interface for wavelength scale phononic devices. One solution to this problem is to use large IDTs followed by focusing elements such as reflections from curved surfaces or propagation through acoustical metamaterials with negative index [15]. This approach, however, increases both the device footprint and insertion loss and adds to the complexity of realizing focusing elements for an acoustical beam of large aperture.

This paper presents a new transducer that directly produces a focused Lamb wave beam in thin piezo-electric membrane. The properties of this beam are completely analogous to Gaussian optical beams produced by laser resonators and can be tailored to produce acoustical beams matched to a given wavelength scale-device. In this work we provide a theoretical description of focused Lamb beams and a design framework for the IDTs that generate them. Experimentally we study the properties of the generated acoustic waves through single and dual port devices. We employ an all-optical scanning confocal balanced homodyne interferometer to perform Doppler vibrometry on the generated focused Lamb beam. We show focusing down to 5 μm from 120 μm long transducers with 85% of the generated acoustical power in the targeted focused mode. Fourier domain analysis is performed to identify the modal composition of the generated beams and understand effects not captured by simulations. For the dual port devices, we study the transmission and reflection properties of these beams as they interact with a sub-wavelength waveguide serving as a hard aperture interjected between send and receive ports and demonstrate minimal impact on insertion and transmission loss.

## II. GAUSSIAN BEAM FORMALISM FOR LAMB WAVES

Efficient coupling to wavelength-scale acoustical structures requires the use of acoustical modes which focus along the propagation direction. The treatment of focusing modes has not been derived in the context of Lamb modes in piezo-electric thin films. Prior work in treating mode propagation in piezo-electric devices has employed reducing exact three dimensional integral equation to analytical expression in two dimensions by ignoring the lateral modal shape [16]–[19]. In the analysis that follows, we go beyond the application of Huygens's principle as was done in [20] and develop a focused beam formalism for acoustical beams which accurately captures the focusing width, divergence, and phase curvature. Toward that end we rely on the optical analog, namely, Gaussian optical beams and follow analogous steps in the derivation. Since Gaussian optical and focused Lamb acoustical beams can both be derived from a wave equation formalism, there are similarities in the mode shapes and propagation properties that we will discuss below. [20], [21]

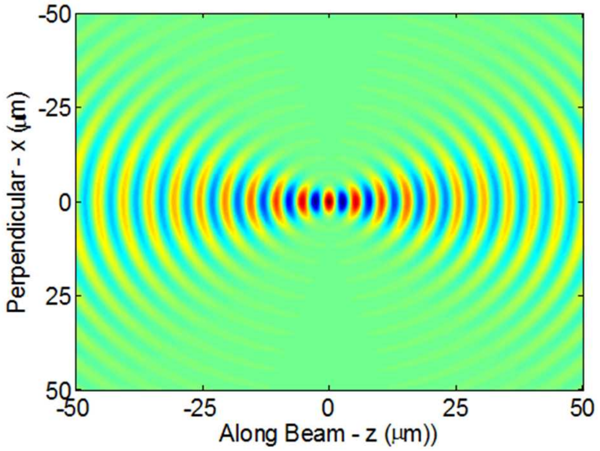

Figure 2. Gaussian Optical beam which results from complex shifting, the Greens function solution of the optical wave equation which is a radially symmetric function of position, $r$, (i.e. setting $z \rightarrow z + iz_0$ such that $r = \sqrt{x^2+y^2+(z+iz_o)^2}$).

Generally speaking, focused mode solutions to time harmonic field equations can be synthesized by a complex translation of the associated Green's function for the corresponding wave equation. For example, the Helmholtz wave equation in an isotropic medium is given by

$$(\nabla^2+k^2)u(r)=\delta(r) \qquad (1)$$

where $k$ is the associated wave-vector, $r$ is distance from the origin, and $\delta(r)$ is Kronecker-delta function. The Green's function solution for the cases of one, two and three dimensions are shown in the Table I [22]. Focused solutions can be derived in two and three dimensions by applying a complex displacement to the Green's function solution. For example, in three dimensions in order to generate a beam propagating along the z axis we set $z \rightarrow z{+}iz_o$, such that $r = \sqrt{x^2+y^2+(z+iz_o)^2}$. This procedure produces a beam as a function of $(x,y,z)$ propagating along the translation axes, $z$, and focused at the origin [21].

In optics, $u(r)$ in the Eq. 1 is the amplitude of the vector potential and is proportional to the transverse electric field in the paraxial limit, where rays that constitute the optical beam

| | Azimuthally symmetric $\nabla^2$ | Green's function |
|---|---|---|
| 1D | $\frac{d^2}{dx^2}$ | $-\frac{i}{2k}e^{-ik\lvert x\rvert}$ |
| 2D | $\frac{1}{r}\frac{\partial}{\partial r}\left(r\frac{\partial}{\partial r}\right)$ | $-\frac{i}{4}H_o^{(2)}(kr)$ |
| 3D | $\frac{1}{r^2}\frac{\partial}{\partial r}\left(r^2\frac{\partial}{\partial r}\right)$ | $\frac{1}{4\pi}\frac{e^{-ikr}}{r}$ |

Table I: Solutions for Helmholz wave equation make small angles relative to the propagation axis. More specifically, in three dimensions, a complex displacement along the z-axis, $z \rightarrow z{+}iz_o$, in the paraxial limit ( i.e. $r = \sqrt{x^2+y^2+(z+iz_o)^2} \rightarrow r = (z+iz_o)+(x\hat{}2+y\hat{}2)/2(z+iz_o)$ ) of the 3D Green's function solution listed in Table I results in the well-known expression for an optical Gaussian beam [21], which is illustrated in Fig. 2:

$$u(z) = \frac{1}{4\pi}\,\frac{e^{-ik(z+iz_o)-ik\frac{x^2+y^2}{2(z+iz_o)}}}{z+iz_o} \tag{2}$$

Here $k = 2\pi/\lambda$ (where $\lambda$ is the wavelength of light), and $z_o$ is the confocal parameter which determines the degree of focusing. Any transverse cross section of the beam has a profile that varies as $\exp[-x^2/w(z)^2]$, where $w(z) = w_0\sqrt{1+(z/z_0)^2}$ and $\pi w_0^2 = \lambda z_0$. $w_0$ is the beam radius at the point of maximum focusing, and $w(z)$ is the beam radius for any cross-section. $\theta_D = w_0/z_0$ corresponds to the divergence angle. The wave fronts of the beam are curved, with a z-dependent radius of curvature given by: $R(z) = z(1+(z_0/z)^2)$. Additionally, the beam experiences a phase shift due to focusing along the direction of propagation known as the Gouy phase shift: $\tan\theta = z/z_o$. The above-mentioned quantities are plotted in Fig. 3 and Fig. 4. For 2D optical beams, the Green's function solution to the Helmholtz wave equation is described by a Hankel function of the second kind, $H_v^{(2)}(kr)$, and can be similarly complex shifted to produce a focused beam in 2D. Although there is no closed form expression, the following asymptotic expansion can be applied which expands a Hankel function of the second kind:

$$H_v^{(2)}(z) = \left(\frac{2}{\pi z}\right)^{1/2} e^{-i(z-\frac{1}{2}v\pi-\frac{1}{4}\pi)}\left[\sum_{m=0}^{p-1}\frac{\left(\frac{1}{2}-v\right)m\Gamma\left(v+m+\frac{1}{2}\right)}{m!\,\Gamma\left(v+\frac{1}{2}\right)(-2iz)m}\right] \tag{3}$$

where Γ(x) is the Gamma function. Retaining only the lowest order term, we arrive at an approximate expression for a 2D focused optical beam in the Gaussian limit, [23]:

$$u_{2D}(z) = \sqrt{\frac{2}{\pi k(z+ib)}}\,e^{-i\left(\frac{k\cdot x^2}{2(z+ib)}-\frac{\pi}{4}\right)} \tag{4}$$

The 2D focused optical beam is similar to the 3D version except for the leading radical which results in the beam waist and radius of curvature begin equal to that of the 3D Gaussian beam, while the Gouy phase shift experiences a factor of ½; $\tan\theta = z/2b$. A comparison is shown in Fig. 3 and Fig. 4.

We can follow the derivation of the Gaussian beam formulation discussed above to arrive at an analogous description of Lamb beams, focused acoustical beam in a slab membrane. The discussion also applies to uniaxial piezo-electric AlN membranes considered in this work which are isotropic in-plane since the coupled quasi-electrostatic and elastic equations can be reduced to elastic equations with modified effectively isotropic elastic coefficients. As such,

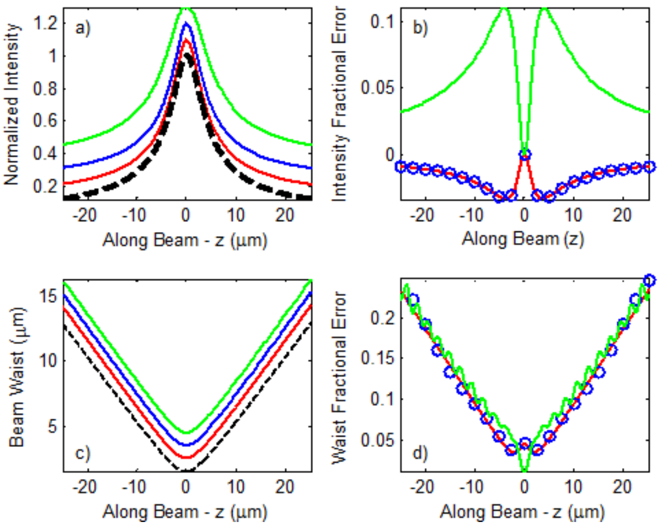

Figure 4. Comparison of on-axis intensity,(a), and beam waist,(c), for a Gaussian optical beam (black), focused 2D optical beam (blue), radial component of focused Lamb beam (red), and out of plane component of the focused Lamb beam (green). (b) and (d) show the fractional error of the normalized intensity and beam waist, respectively, from that of a Gaussian beam. All curves in (a) and (b) are offset for clarity and have intensity of 1 at z=0 and a beam waist of 5µm. Blue circles are chosen for clarity in (b) and (d).

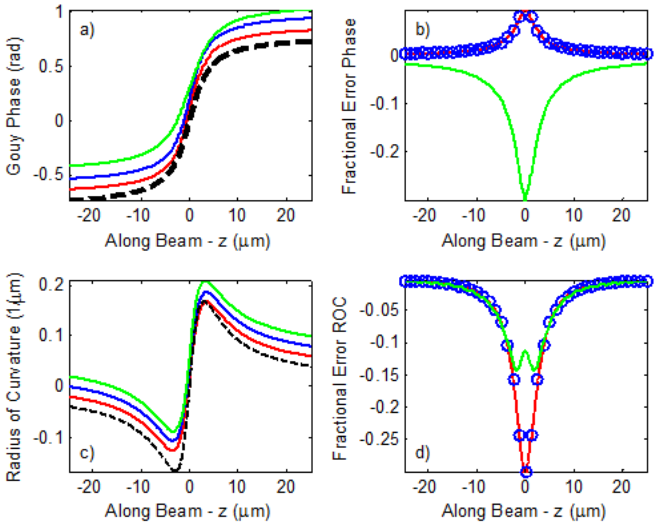

Figure 3. Comparison of Gouy phase (a), and radius of curvature (c), for Gaussian optical beam (black), focused 2D optical beam (blue), radial component of focused Lamb beam (red), and out of plane component of the focused Lamb beam (green). (b) and (d) show the fractional error of the Gouy phase and radius of curvature, respectively, from that of a Gaussian beam. Curves in (a) and (c) are offset for clarity and corresponded to beams with a 5µm waist. Blue circles are chosen in (b) and (d) for clarity.

Lamb waves in isotropic materials are solutions to the acoustical field equations in thin films which satisfy:

$$(\nabla^2+k^2)\Delta = 0$$
$$\Delta = \frac{\partial u_r}{\partial r}+\frac{u_r}{r}+\frac{\partial u_z}{\partial z} \tag{5}$$

where Δ is the dilation, and the gradient operator, ∇, is expressed in 2 dimensions, [24], [25]. The dilation therefore is the analogous quantity to the vector potential amplitude for optical beams. The solution to the above equation in terms of dilatation is the 2D Green's function solution of the Helmholtz wave equation given in Table 1. To arrive at the displacement amplitude $u$, the dilatation needs to be integrated. This results in a displacement field distribution in cylindrical coordinates given by:

$$ue^{-i\omega t} = \hat{\boldsymbol{r}}\alpha_{p,m}(y)J_0(kr) + \hat{\boldsymbol{z}}\beta_{p,m}(y)J_1(kr) \tag{6}$$

where **r** is the radial component and **z** is the out of plane component in cylindrical coordinates, $J_0$ and $J_1$ are Bessel functions of the first kind, and the functions $\alpha_{p,m}(z)$ and $\beta_{p,m}(z)$ are trigonometric functions of **z** that satisfy open boundary conditions and account for modes that are higher order along the film thickness [25]. The above equation is the vector Green's function solution for displacement amplitude for acoustical fields in thin films. A complex translation along one axis for both radial and out-of-plane components will yield the mathematical description of a focused lamb wave beam.

A complex translation of Equation 6 involves shifting both first and second order Bessel functions, which complicates deriving expressions for the beam radius, curvature, and Gouy phase shift. Bessel functions, $J_v(z)$, however, can be related to each other by considering the following well known asymptotic expansions, [26], [27]:

$$\begin{aligned} &J_v(z) \\ &= \left(\frac{2}{\pi z}\right)^{1/2} \left[ cos\left(z - \frac{1}{2}v\pi - \frac{1}{4}\pi\right) \sum_{m=0}^{p-1} \frac{(-1)m(v,2m)}{(2z)m} \right. \\ &\left. - sin\left(z - \frac{1}{2}v\pi - \frac{1}{4}\pi\right) \sum_{m=0}^{p-1} \frac{(-1)m(v,2m+1)}{(2z)^{2m+1}} \right] \end{aligned} \tag{7}$$

where $(v, 2m)$ and similar expressions are combinatorial functions (i.e. $v$ choose $2m$). The above equation can be further expanded using Euler relation to yield:

$$\begin{aligned} J_v(kr) = &\left(\frac{1}{2\pi kr}\right)^{1/2} \\ &\times \left[ e^{i\left(kr - \frac{1}{2}v\pi - \frac{1}{4}\pi\right)} \left(1 + \frac{i}{kr} + \frac{1}{kr^2} + \cdots\right) \right. \\ &\left. + e^{-i\left(kr - \frac{1}{2}v\pi - \frac{1}{4}\pi\right)} \left(1 + \frac{i}{kr} + \frac{1}{kr^2} + \cdots\right) \right] \end{aligned} \tag{8}$$

For loose focusing, $r$ becomes sufficiently large that only the lowest order term will dominate. Thus, imparting a complex displacement, ($z \rightarrow z + ib$), to Equation 6 and retaining only the lowest order terms from Equation 8, we arrive at the focused solution for acoustical beams in the Gaussian limit:

$$\begin{aligned} u = &\hat{\boldsymbol{y}}\alpha_{p,m}(y)\frac{1}{4\pi} \frac{e^{-ik(z+jb)-ik\frac{x^2+y^2}{2(z+jb)}}}{\sqrt{z+jb}} \\ &+\hat{\boldsymbol{z}}\beta_{p,m}(y)\frac{e^{-ik(z+jb+\frac{1}{2}\pi)-ik\frac{x^2+y^2}{2(z+jb)}}}{\sqrt{z+jb}} \end{aligned} \tag{9}$$

Both the radial and the out-of-plane component of the Lamb beam approach expressions for the field amplitude of a 2D focused optical beam in the Gaussian limit (see Equation 4) but are phase shifted with respect to each other by a factor of $\pi/2$. Focused Lamb-wave beam profiles, therefore, converge to 2D focused optical beam profiles in the limit of loose focusing and far from the beam center. A comparison of all beams discussed is shown in Fig. 3 and Fig. 4 which show results for a 3D Gaussian optical beam, 2D focused optical beam, and the radial and out-of-plane components of a focused acoustical Lamb Beam. Differences between these beams are most prominent under tight focusing, and the beams converge to each other under loose focusing. Additional error correction terms for acoustic beams described by Equation 9 can be derived from higher order terms of Equation 8 where each error term has the form:

$$u_{error} = \frac{e^{+/-ik(z+jb)-ik\frac{x^2+y^2}{2(z+jb)}}}{\sqrt{z+jb}^{m}} \tag{10}$$

and thus can be interpreted as a higher order correction beam. For tight focusing where the error terms will more strongly contribute, the overall acoustical beam will focus, but amplitude and width modulations will appear along the axis of propagation for tighter focus, as shown by the wiggles in Fig. 3(d). These error terms however are small.

Thus, the mathematical form of an optical focused beam in two and three dimensions and a focused acoustical beam in a thin film are similar and can be related through asymptotic expansion of Bessel and Hankel functions. All beams converge to a spot with constant phase and diverge with increasing waist, converging to a fixed divergence angle. The focused Lamb beam is expressed as a zeroth order beam plus higher order correction beams. For the zeroth order beam, the waist, radius of curvature and Gouy phase shift can be expressed as functions of a confocal parameter and are given by:

$$\left.\begin{aligned} w(z) &= w_0\sqrt{1+\left(\frac{z}{z_0}\right)^2} \\ R(z) &= z\left(1+\left(\frac{z_0}{z}\right)^2\right) \\ \tan\frac{\theta(z)}{2} &= \frac{z}{z_0} \end{aligned}\right\} \tag{11}$$

where, the beam waist, $w_0$, the confocal parameter, $z_0$, and the far field divergence angle, $\theta_D$, are expressed as,

$$\left.\begin{aligned} \pi w_0^2 &= \lambda z_0 \\ \theta_D &= \frac{w_0}{z_0} \end{aligned}\right\} \tag{12}$$

The above equations are used in the next section to facilitate design of transducers that generate focused Lamb beams.

## III. FOURIER DOMAIN TRANSDUCER DESIGN

Straight IDTs generate straight crested planar lamb waves by imparting a modulating compressive stress profile in the immediate vicinity of the metal/piezo-electric bonding interface that aligns with linear constant-phase contours of the output wave. In principle curved IDTs can provide a greater diversity of mode shapes[25], [28]. However, with constant width IDTs, the generated waves correspond to eigen-modes of the elastic wave equation only in the case of straight or circular configurations; where straight IDTs produce plane waves, and circular rings produce Bessel-like modes (Equation 6 above). In both cases the generated waves have constant amplitude along phase fronts. The focused beams described in the previous section, however, have wave amplitudes that vary along constant phase contours, having a maximum along the propagation axis. To generate such beams, the IDTs must be spatially varying along the transducer length. In the following, we show how to properly modulate the transducer width along the transducer length in order to generate the focused Lamb beams discussed in the previous section.

A single finger IDT on a thin film piezo-electric material with a grounded bottom metal layer and an infinitely long top electrode actuated by a temporally sinusoidal voltage with angular frequency $\omega$ couples to Lamb wave modes and produces forward and backward-going waves as illustrated in Fig. 5. The electrical excitation for a single finger is analogous to the case where a bulk wave is excited by a spatially uniform (in x and y) and temporally sinusoidal volumetric force in the limit where fringing fields are neglected in which case the amplitude of the forward and backward going waves are given by [13]:

$$a^{\pm}(z) = \pm F\frac{2F}{\omega/V_l}\sin\left(\frac{\omega L}{V_l}\right)\bar{U}\exp(\mp i\omega t) \qquad (13)$$

where $F$ is the force density, $V_l$, is the speed of sound, $\omega$ is the angular frequency $\bar{U}$ is the voltage amplitude $z$ is the distance from the electrode mid-point, and $l$ is the electrode width. The amplitude of the emitted wave is therefore related to the electrode with for a single finger IDT and is proportional to $\sin(kL)$ where $k = \omega/V_l$.

For spatially varying IDTs, we expect that the field amplitude of waves emitted in the immediate vicinity of the IDT section under consideration to be determined by the width and normal along the transducer length as long as the electrode width and direction vary slowly compared to the wavelength. In other words, we expect the local amplitude to vary as:

$$a_{\mathrm{local}}(s)^{\pm} = \gamma V_0 \sin kL_{\mathrm{local}}(s) \qquad (14)$$

where $s$ is the position along the electrode with and $\gamma$ is a constant of proportionality determined by the film thickness and material properties. Within the limits of this *local approximation*, a transducer can be tailored to emit the focused Lamb beam described in the previous section, by varying the transducer width to follow the Lamb beam amplitude along constant phase contours. In the Gaussian beam limit for large z, (i.e. far from the focus with $|z| \gg z_0$, where $z_0$ is the confocal parameter described in the previous section), the field has an on-axis peak amplitude inversely proportional to the beam waist at z, i.e. $A_{\max}/w(z)$, and decays from its on-axis maxima as $\exp\left[-\theta^2/{\theta_D}^2\right]$. Thus, a single finger placed far to the left of the focus and having an on-axis local-width maximum which decays as $\exp\left[-\theta^2/{\theta_D}^2\right]$, will produce a wave that has a focus at the origin.

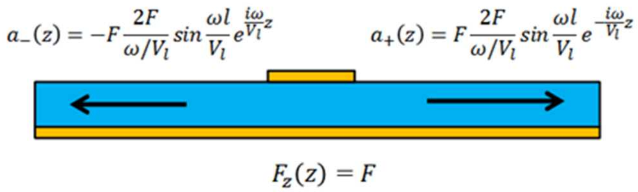

Figure 5. Excitation of a thin film piezoelectric field by an IDT with a bottom metal ground plane, which is analogous to excitation of a bulk wave by a spatially uniform (in *x* and *y*) and temporally sinusoidal volumetric force in the limit where fringing fields can be neglected.

A single curved finger would have an electrical impedance similar to that of a single straight finger of equal area. Thus, a set of curved IDTs is required to achieve reasonable filter quality factors and impedance matching. We specify a set of electrode fingers by placing the first finger (the 0th finger) an integer multiple of wavelengths to the left of the origin at a coordinate -$\bar{z}_0$. Additionally, the 0th finger will have an on axis width of $L_0 = \lambda/2$. Each successive finger will have a center at $\bar{z}_n = -\bar{z}_0 - n\lambda$ and an on-axis width falling inversely with radius to maintain constant electrode area for each finger. Off-axis, all fingers require their local widths to fall off exponentially following the amplitude of the Lamb beam. Thus $L_n(\theta) = L_n(0)\,\exp\left[-\frac{\theta^2}{{\theta_D}^2}\right]$, with $L_n(0) \sim \frac{1}{nL_0(0)}$. Additionally, there is a maximum angle, $\theta_D/2$, out to which the fingers are swept which ensures that all the fingers meet the bus at a straight line.

We can more generally address beam shapes produced by width-modulated, curved transducers by viewing points on a transducer as source points for locally straight crested waves as implied by Equation 14 [13], [20]. Consider the field amplitude generated from a single ring transducer with an angle dependent local width, as illustrated in Fig. 6. Integrating along the ring, the displacement field at an arbitrary point can be expressed as:

$$u(r,\theta') = \int A(\theta)\exp\left[i\vec{\boldsymbol{k}}\cdot\left(\vec{\boldsymbol{r}} - \vec{\boldsymbol{R}}\right)\right]d\theta \qquad (15)$$

Where $A(\theta)$ is the amplitude generated by the IDT within the assumptions of the local approximation in Equation (14). Expanding vector quantities in the above expression and using trigonometric identities we can arrive at the following:

$$\begin{aligned} u(r,\theta') &= \exp(-ikR) \\ &\times \int A(\theta)\exp(-ikr\cdot\cos(\theta'-\theta))\,d\theta \end{aligned} \qquad (16)$$

which relates the displacement field to the convolution between the angular-dependent local amplitude which is a function of the local width and a complex exponential. Equation 16, can be related to a 2D Fourier transform, expressed in cylindrical

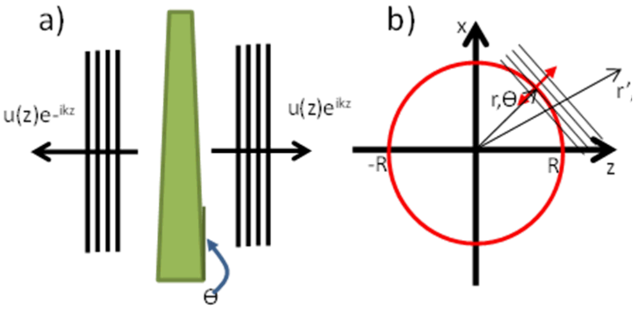

Figure 6. a) In the local width limit, a portion of transducer can be viewed as a plane wave source with amplitude proportional to the local transducer width and normal to the transducer length. b) The field at a given point r', Θ' from a circular IDT with angular dependence width can be determined by integrating the local contributions along the ring contour.

coordinates, which is given by:

$$
\begin{aligned}
&f(r,\theta) = \mathcal{F}^{-1}\{F(\rho,\varphi)\} \\
&= \int_0^{2\pi}\int_0^{\infty} F(\rho,\varphi) exp(-ik\rho r\, cos(-\theta))\ \rho d\rho\, d\varphi
\end{aligned}
\tag{17}
$$

where $r$ and $\theta$ represent radius and angle in cylindrical coordinates in the spatial domain; and ρ and φ represent radius and angle in cylindrical coordinates in the Fourier domain, i.e. k-space [29].For functions having only angular dependence in k-space, the Equation (17) can be further simplified as follows:

$$
\begin{gathered}
F(r,\theta) = F(\theta) \times \delta(k - k_o) \\
f(r,\theta) = \int_o^{2\pi} d\emptyset\, k_o F(\theta) \exp\big(-ik_o r cos(\emptyset - \theta)\big)
\end{gathered}
\tag{18}
$$

Comparing Equations 16 and 18 above we can see the correspondence of the local amplitude of circular transducers, *A(θ)*, to the Fourier amplitude, *F(θ)*, for functions comprised by rings in k-space. Thus, we can specify the amplitude profile of the wave emitted from circular transducers by considering their representation in the Fourier domain. Additionally, concentric rings of transducers can be used to increase signal strength and electrical impedance. Fields from concentric rings can be coherently combined as indicated by the radial phase factor in Equation 16.

Consider the case where A(θ) = $F(k) = \delta(k - k_o)$. This corresponds to a physical transducer which is a ring of constant width. From well-known Fourier transform pairs it is clear that the amplitude of the emitted wave will be: $u = f(r,\theta) = J_o(k_o r)$. Thus, from the perspective of Fourier transform pairs, a circular transducer of constant width will excite a Bessel beam as indicated in Fig. 7(a) and 7(b). This agrees with what we expect given Equation 7, the Green's function solution of the acoustical wave equation in cylindrical coordinates. Following the analytical method described in the previous section, a complex shift in the direction of propagation is required in order to generate focused beams from Green's functions solutions. Thus, a complex shift of the physical transducer that generated the Bessel mode will yield the desired focused beam. A real valued shift is expressed in the Fourier domain as a varying phase [30]. The rule still applies if the shift is complex. Thus, applying properties of Fourier transforms we have:

$$
\begin{gathered}
\mathrm{f}(\vec{R} + \overrightarrow{R_0}) \leftrightarrow \exp(-i\vec{k}\cdot\overrightarrow{R_0}) \times \mathrm{F}(\vec{k}) \\
\mathrm{f}(\vec{R} + iz_0\hat{\mathbf{z}}) \leftrightarrow \exp(-z_0 k_o cos\theta) \times \mathrm{F}(\vec{k})
\end{gathered}
\tag{19}
$$

The Fourier domain function then becomes: F(Θ)=$\beta$exp$(-z_0 k_o cos\theta)$×δ(k-k$_o$) and the corresponding local amplitude becomes:

$$
A(\theta) = \beta \exp(-z_0 k_0 cos\theta) \tag{20}
$$

where $z_0$ is the confocal parameter in Equations 11 and 12. These steps are illustrated in Fig. 7(c) and 7(d). Using Equations 14 and 20 to relate the local amplitude to the local transducer width, we arrive at the necessary condition for the local transducer width for a ring IDT to form a Bessel beam:

$$
L(\theta) = \frac{\pi}{k_0} sin^{-1}(\exp(z_0 k_0(1 - cos\theta))) \tag{21}
$$

Thus, circular transducers designed with Equation 21 will yield focused Lamb beams. Additionally, concentric rings of transducers separated by integer multiples of the excitation wavelength can be used to coherently interfere focused beams generated from each ring, in order to achieve electrical impedance matching, although the widths should be scaled such that the area of each finger is the same.

From the perspective of Fourier domain transducer design, the influence of a finite aperture can be viewed as multiplying the Fourier domain with a rectangular windowing function, which in the spatial domain acts as convolving with a *sinc* function, thus spreading the energy at the focus by an amount proportional to the aperture size. We also note here that the above analysis is valid in the plane-wave limit of point sources [21]. Acoustical points sources not in the far-field limit are better described as emitting circular waves which drop in

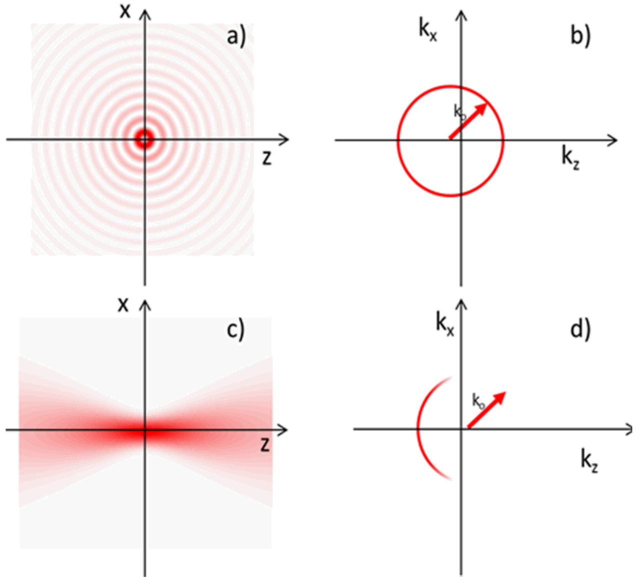

Figure 7. Fourier transform pairs leading to transducer design. The Bessel function in (a) consists of a ring in k-space (b). A complex translation of the Bessel function leads to the focused beam in (c) whose k-space composition is confined to a ring but has an angular intensity modulation superimposed.

amplitude as *1/r*. Thus, transducers designed too close to the focus point in the near-field will have deviations from the above analysis that originate from point sources better described as a circular wave in two dimensions. However, for the cases discussed in this work with slowly varying local widths and transducers placed sufficiently far from the focus, the Fourier domain view of circular transducers remains valid.

## IV. FINITE ELEMENT SIMULATION

Employing the curved transducer design methodology described in the previous section, we developed and performed finite element method (FEM) simulations in COMSOL for a transducer capable of producing a focused beam. We choose a design frequency of 2GHz in a 750 nm thin film of aluminum nitride so that $k_0=2\pi/5.1\mu m$. A confocal parameter of $z_0=11$ μm was selected so that the focused waist of a beam emitted from a single transducer is 5 μm. Additionally, a transducer aperture of $\theta_D = 1.5$ rad and 18 fingers were chosen so that the electrical impedance between the figures and ground plane was nearly matched to 50Ω.

A piezo-electric FEM model of the transducer is shown in Fig. 8. The wave is excited by an oscillatory voltage applied between the fingers (outlined in black) and a ground plane on the bottom face of the membrane. The bus is not included in the simulation. The left-hand boundary is free and serves as a back reflector making the transducer single-ended. The other boundaries are adiabatic absorbers, which have been separately verified to absorb without significantly reflecting back into the simulation.

The transducer design does indeed produce the expected focused Lamb beam, which is localized to a minimum spot-size that agrees with that predicted by the theory and also focuses to the correct distance from the right-most transducer. The theoretical framework utilizes a plane wave basis of radial displacement, essentially ignoring the vertical dependence of the displacement field. Therefore, the relevant displacement field for comparison in the full 3D simulation is the radial component at the mid-plane between the top and bottom electrodes where the field amplitude is the largest. Fig. 9 shows a comparison of the amplitude predicted by the theoretical model and the radial displacement field of 3D FEM simulation at the mid-plane. The close agreement confirms the analysis in the previous section.

Although the FEM simulation is three-dimensional, analysis of 2D planar sections for a fixed vertical position can be matched with the theoretical framework developed in the previous section. This approach is valid because the z-dependent variations of the beam solution can be factored. Further analysis of the simulation is conducted by considering the Fourier domain composition of the simulated beam profile. As shown in Fig. 10, the Fourier transform intensity profile is constrained on rings in k-space, which decay exponentially as the θ deviates from –π. Energy not constrained on a ring represents deviations from the idealized case. The angular dependence of the Fourier amplitude along the dominant circular contour is shown by the blue curve in Figure 11. The intensity profile along the circular contour matches the theory (black curve) including the sharp cut-off due to the bus.

The region in Fig. 10 outside the dashed circle shows the amplitude outside the central ring magnified by a factor of 1000. The presence of an additional ring indicates that a higher order beam is very weakly excited. By integrating regions in k-space, the FEM simulation results enable characterization of modal excitation efficiency. The majority of the drive frequency is directed to the fundamental mode in that 85% of

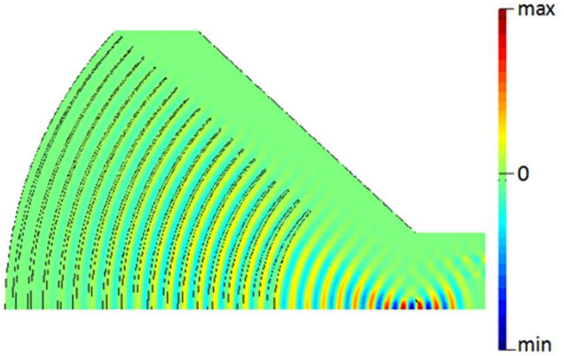

Figure 8. Piezo-electric FEM model of a unidirectional Gaussian Lamb beam with angular aperture $\theta_D$=1.5, produced by driving an array of width modulated IDTs with a harmonic potential at its resonance frequency. The first finger starts at 10 wavelengths back from the origin.

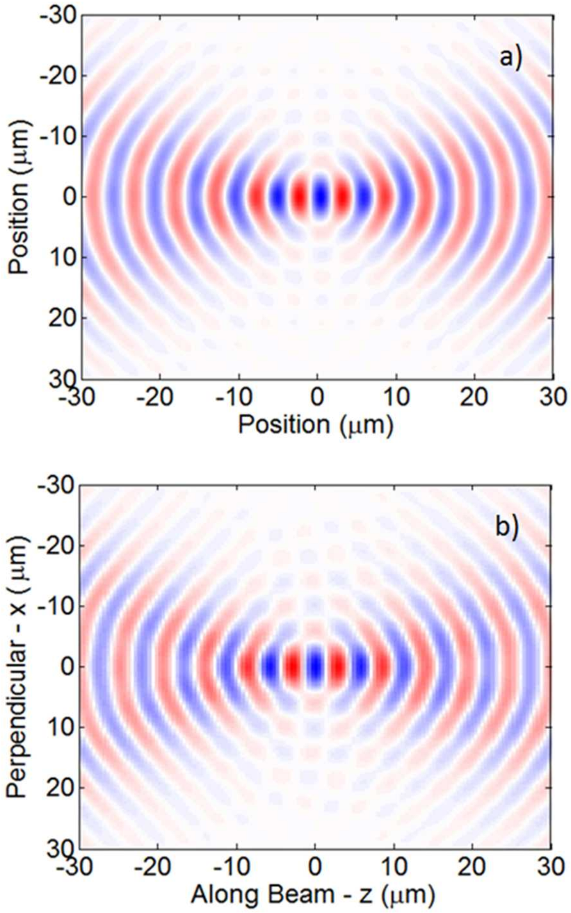

Figure 9. a) Field profile from theoretical model. b) Field profile of radial displacement at the AlN membrane mid-plane from 3D piezoelectric FEM model.

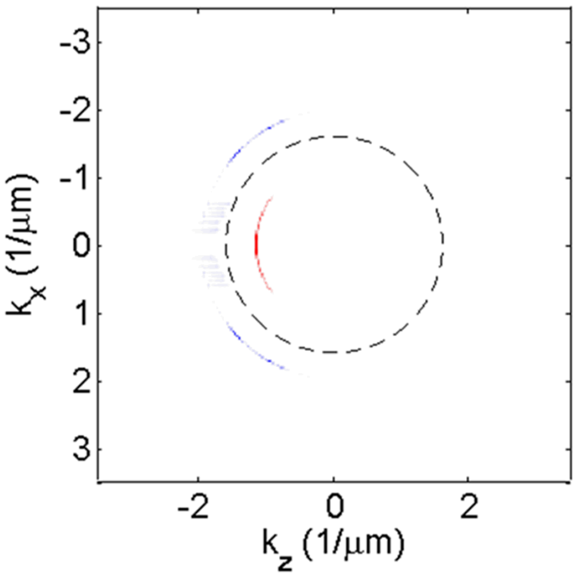

Figure 10. Two dimensional Fourier Transform of radial displacement at the central cross-sectional plane of the simulated thickness. The portion outside the dashed line is magnified by 1000 times.

the energy resides in the inner ring. Less than 1% resides in the outer ring, and the remaining 14% is dissipated isotopically.

The 3D FEM model, allows us to look at the z-component of the displacement field at the bottom-plane, which is the field component accessible to optical investigation and will be compared to experimental data in a later section. A Fourier domain analysis shows that energy is confined to a ring in k-space similar to Fig. 10. The red curve in Fig. 11 plots the angular dependence of the intensity in k-space along that ring. The profile which contains wings around the central coordinate is notably different than the mid-plane curve, although both are generated from the same mode. Thus, interrogation of the z-component of the displacement field at the bottom-plane must account for the non-uniform mapping to radial mid-plane displacement for a proper comparison to theory. This consideration will be relevant in a later section pertaining to confocal imaging.

Fig. 12 plots the displacement amplitude in the mid-plane and the z-component at the bottom plane at the focus position and also along the beam propagation direction. The agreement of the curves indicates that the theory of the previous section accurately predicts the focusing action of the transducers as described by Fourier domain amplitude control. Here we have simulated focusing to a 5μm spot. The bottom-plane displacement shows considerable structure, although the mid-plane displacement is smooth. This again illustrates the fact that the mid-plane displacement represents the beam composition and the bottom-plane alone will contain artifacts. Thus, measurements of the bottom plane need to account for the mapping of bottom-plane to mid-plane displacement. This fact

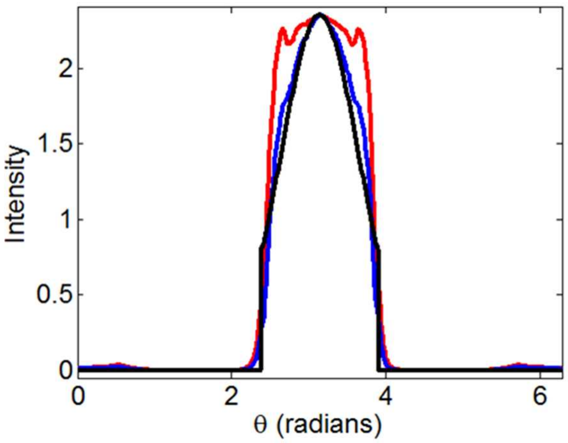

Figure 11. Angular dependence of Fourier amplitude. Black curve is predicted from theory. Blue curve is from the radial component at the mid-plane of the FEM simulations and corresponds to the inner ring in Figure 10. Red curve is from the vertical component at the bottom-plane. Amplitude components centered around π correspond to forward propagating Lamb waves while those centered around 0/2π correspond to backward propagating waves.

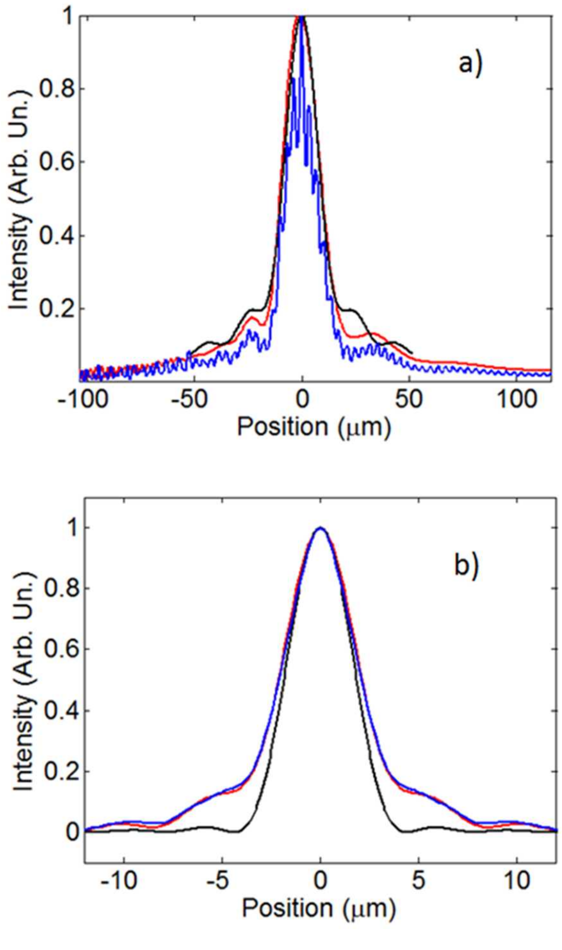

Figure 12. Comparison of displacement intensity profiles for focused beam for analytical (black) and radial component of the FEM simulation at the mid-plane (red) and bottom-plane (blue), which is experimentally accessible, showing excellent agreement, justifying a two-dimensional analytical theory and the fact that the mid-plane displacement represents beam composition while the experimentally accessible bottom-plane contains artifacts. (a) Intensity profile of displacement along center of beam in the propagation direction. Ripples appear in the field amplitude at the bottom plane. b) Intensity profile of displacement for cross section at focus position illustrating the beam waist. The simulated waist has a broad pedestal originating from the finite transducer aperture.

is particularly relevant in the experimental section where we measure the bottom-plane displacement. Additionally, Fig. 12(a) shows the axial variation of the displacement is slightly asymmetric with respect to the focus. This is due to the fact that points on the transducers emit circular waves with intensity falling inversely with distance rather than plane waves as was mentioned in Section III.

## V. FABRICATION

The fabrication steps used to realize the transducers followed a standard AlN process developed at Sandia National Labs, [31] and the key steps are illustrated in Fig. 13. The process begins with high resistivity six-inch Si wafers upon which a 0.6 μm oxide and a 4 μm polysilicon release layer are consecutively deposited. The polysilicon is then patterned to define where the AlN membranes will be undercut and suspended from the substrate. This is shown in Fig. 13(a). The polysilicon in this layer will be selectively removed in later steps, and therefore constitutes a sacrificial material that ultimately defines regions of air.

Next, an oxide layer is deposited and chemically and mechanically polished squaring up to the sacrificial polysilicon release material. Additionally, in this layer, tungsten plugs are machined into the oxide in order to make contact to the bottom electrode. This is shown in Fig. 13(b). Ultimately, electrical pads will be connected from above to the tungsten plug through vias. This layer, therefore, constitutes regions of tungsten plugs over which vias will ultimately land, and regions of the suspended membrane where polysilicon is defined. Next, the electrically grounded bottom electrode, formed from 20/20/50 nm of Ti/TiN/Al is deposited, patterned and a 0.75 μm layer of AlN is sputter deposited as shown in Fig. 13(c). Vias are then etched in the AlN landing on the tungsten plugs. After this, a top electrode layer of 70/20 nm of Al/TiN is deposited. The resulting stack is shown in Fig 13(d).

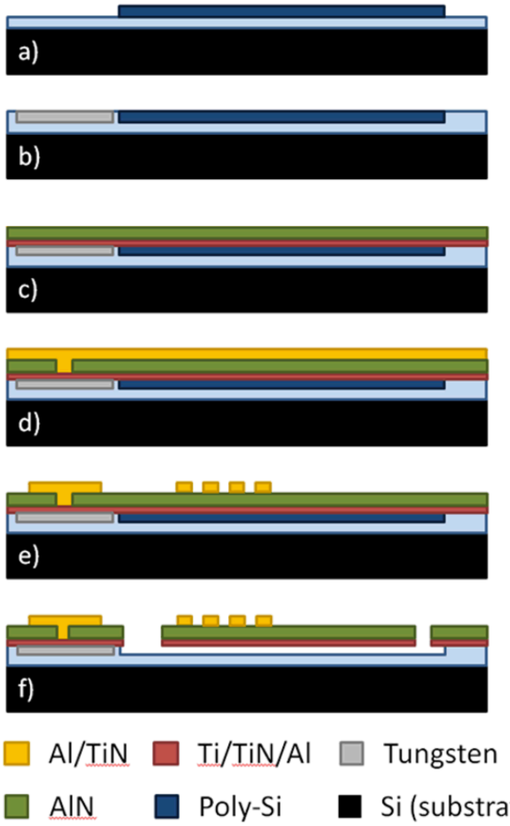

Figure 13. Key fabrication steps. a) Poly-Si patterned to define the release layer. b) Tungsten plug stop for electrical via c). Aluminum Nitride layer deposited. d) Contact to bottom metal. e) Top electrodes patterned. f) Poly-Si layer removed with $XeF_2$ release.

The top electrode layer is then patterned to form the piezo-electric transducers and pads as shown in Fig. 13(e). Release trenches are finally etched through the AlN and bottom metal to expose the polysilicon release layer and simultaneously create the back reflectors and/or waveguides. The device is suspended from the substrate using a dry release in XeF2. An example a one-port device is shown in Fig. 14.

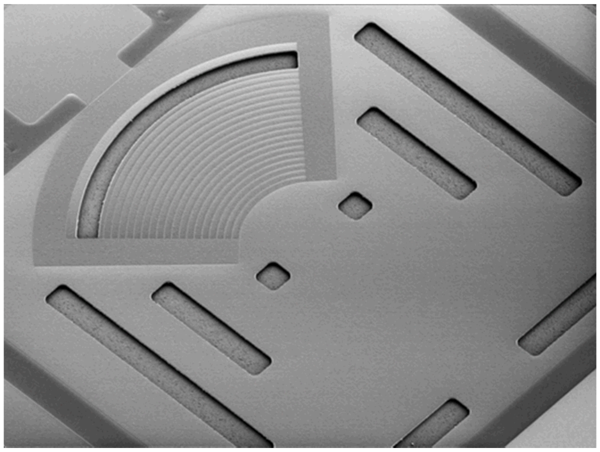

Figure 14. SEM of single-port Gaussian Lamb transducer device in AlN.

## VI. OPTICAL AND ELECTRICAL CHARACTERIZATION OF ONE-PORT DEVICES

In this section we experimentally evaluate one port devices by imaging the displacement field profile and comparing it to the developed theory. Additionally, we look at the k-space composition of the measured field to understand which modes are excited by the designed transducer and estimate the excitation efficiency in the desired mode and spurious modes. As will be shown below, k-space analysis is useful to understand the actual excitation efficiencies since: the measurement tool only senses out of plane displacement, and so vertical modes show up strongly even though they contain relatively little acoustic energy. K-space analysis enables us to discriminate between modes and estimate actual efficiencies based on well-established theoretical calculations of vertical displacement to forward going power as a function of mode type.

The one port-devices shown in Fig. 14 consisting of a single focusing transducer with back reflector were designed with long open areas for the wave to propagate unobstructed, which allows us to optically test the transducer and visualize the beam formation. Electrical $S_{11}$ measurements, shown in Fig. 15, were

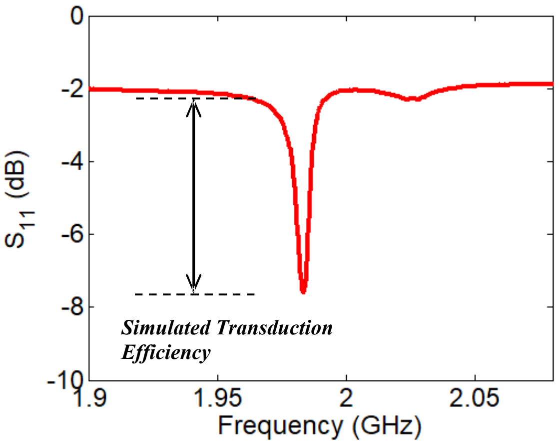

Figure 15. S11 measurement of the single port focusing transducer depicted in Fig. 14 which agrees with the simulated transduction efficiency.

performed and we measured an approximately 50% transduction efficiency of RF to acoustical energy, confirming the prediction from FEM simulations.

We employed a scanning confocal balanced homodyne interferometer to perform Doppler vibrometry on AlN membranes in order to image the bottom-plane displacement of the excited acoustical modes, [32], [33]. A schematic of the interferometer is shown in Fig. 16. Essentially, the setup is a balanced homodyne interferometer operating at 1550 nm. A balanced pair of photodiodes measures the difference in optical power at the output ports of a Mach-Zehnder interferometer (MZI) consisting of a local oscillator (LO) path and a weak probe path, where the path of a weak probe (more than 10 dB down in power from LO) includes a bounce off the metalized bottom surface of the membrane. An anti-reflection coated lensed tapered fiber (LTF) and magnetic circulator allow the path of the MZI probe arm to focus light down to a nearly diffraction-limited spot (2 um diameter) and collect the reflected light with very high efficiency (~95% one-way loss through the LTF). Because the bottom electrode of the device is a continuous film of aluminum with 99% reflectivity at 1550 nm, the system will efficiently measure the change in path length due to fluctuations induced by propagating Lamb waves. Since the change in refractive index in the AlN membrane is negligible, the optical phase change will be dominated by the movement of the bottom metal. Thus, the system is highly sensitive to out-of-plane displacements of the bottom metal induced by Lamb waves propagating through the membrane.

A network analyzer simultaneously drives the device transducer while coherently demodulating the signal from the interferometer, which allows phase-coherent detection of the Lamb waves propagating through the membrane. By scanning the LTF over the surface of the device at a fixed height (and with 10 nm in-plane resolution), we can fully reconstruct the amplitude and phase of the Lamb waves in the device with a signal-to-noise ratio often in excess of 60 dB with sufficiently low RF drive power to avoid thermal effects. Fig 17. shows a displacement amplitude image collected from the device shown in Fig. 14 when driven with 0 dBm at ~2 GHz corresponding to an acoustical wavelength of $\lambda = 5.1\ \mu$m. The mode produced by the transducer shows the focusing of an acoustical beam to a minimum waist and subsequent diffraction, thus capturing the essential features and functionality previously described. There is however, the notable presence of prominent interference fringe pattern in the data.

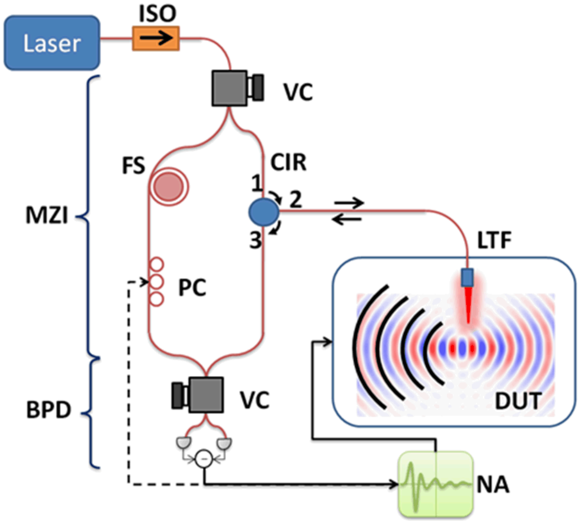

Figure 16. Schematic diagram of scanning confocal balanced homodyne interferometer used to optically characterize Lamb wave devices. MZI: Mach-Zehnder interferometer, BPD: balanced photodetector, PC: polarization controller. ISO: optical isolator, FS: fiber stretcher, VC: variable coupler, CIR: circulator, LTF: lens taper fiber, NA: network analyzer.

The origin of the fringe pattern in Fig. 17 can be understood by examining the energy distribution in the Fourier domain (k-space) shown in Fig. 18. The energy is confined to concentric rings consisting of an inner and an unexpected outer ring. The inner ring with a radius of 1.1 $\mu m^{-1}$ corresponds to the k-vector amplitude of the desired excited mode, the symmetric mode. The outer ring, which is responsible for the fringe corresponds to an additional mode of a larger k-vector at the same frequency.

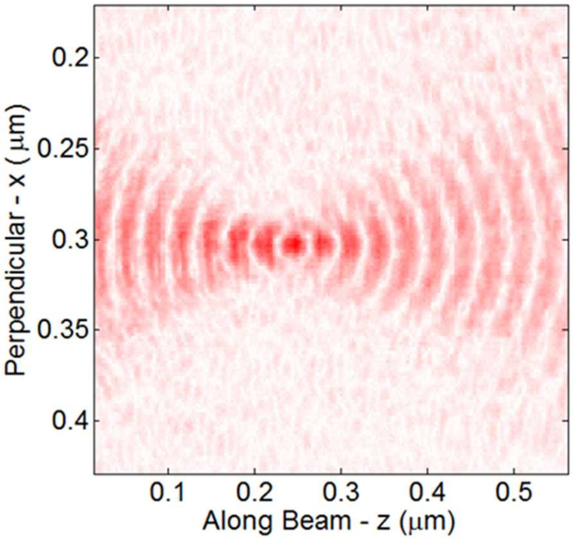

Figure 17. Amplitude of optically measured beam. Intensity corresponds to out-of-plane displacement at the bottom of the membrane. Prominent fringes are visible and due to excitation of anti-symmetric mode.

We can identify this mode by considering the dispersion relations for the AlN membrane. Fig. 19 and Fig. 20 show the dispersion relation and mode profiles, respectively, as determined from finite element modeling. As indicated, for the given frequency of 2GHz, a symmetric, anti-symmetric, and shear mode exists. The radius of the inner ring corresponds to the symmetric mode k-value of 1.25 $\mu m^{-1}$ while the outer ring corresponds to the anti-symmetric mode with a k-value of 3.15 $\mu m^{-1}$. The shear mode is not present as indicated by the absence of a ring at 2 $\mu m^{-1}$. Thus, the presence of an outer ring indicates the excitation of the lowest order anti-symmetric mode by the designed transducer.

Analysis in k-space, in general, provides a prescription to deconstruct the transduction process by identifying the classes of modes involved. Care needs to be employed, however, when attempting to extract relative excitation efficiencies of each mode by integration along the corresponding contours in k-space. For the case in Figure 18, the energy of inner ring contains approximately 1.7 times that of the outer ring. The 2D analysis, however exaggerates the relative amplitudes for the three-dimensional modes since the majority of the displacement occurs in-plane at the center of the membrane in the radial direction, while the imaging setup detects only out out-of-plane displacement at the bottom of the membrane.

The ratio of total out-of-plane displacement at the bottom-plane to total radial displacement at the mid-plane for a focused acoustical beam formed with the lowest antisymmetric mode is much larger than then for the lowest symmetric mode. The mode profiles for the symmetric, antisymmetric and shear modes at 2GHz are shown in Fig. 20. The modal excitation efficiency can then be estimated by integrating energy in a contour and scaling appropriately to get the forward going power. These factors were determined from FEM simulations. The fraction of energy in the vertical component for each mode is .3%, 73%, and 0% respectively. The measured situation here thus corresponds to 85% of the three-dimensional mode power occurring in the desired symmetric mode. Thus, the above results indicate that we have successfully focused the acoustical energy down to 5μm with 85% of the transduced RF energy delivered to the targeted lowest-order symmetric-mode.

Since the symmetric and anti-symmetric modes appear as rings of different radius in the k-space, the modes can be filtered spatially to allow fair comparison to theory. Figure 21(a) shows the amplitude of the field isolated inner ring compared to the FEM model. We note that although the bottom-plane vertical displacement for the FEM shows structured profile before and after the focus with additional ripples through the focused region, the mid-plane radial displacement which contains the majority of the energy faithfully conforms to that of a focused Lamb beam. The vertical displacement field at the bottom-plane must be mapped to the field at the mid-plane in order to accurately characterize the generated beam.

Although there is qualitative agreement, the experimental data appears less focused. This is confirmed by looking at the

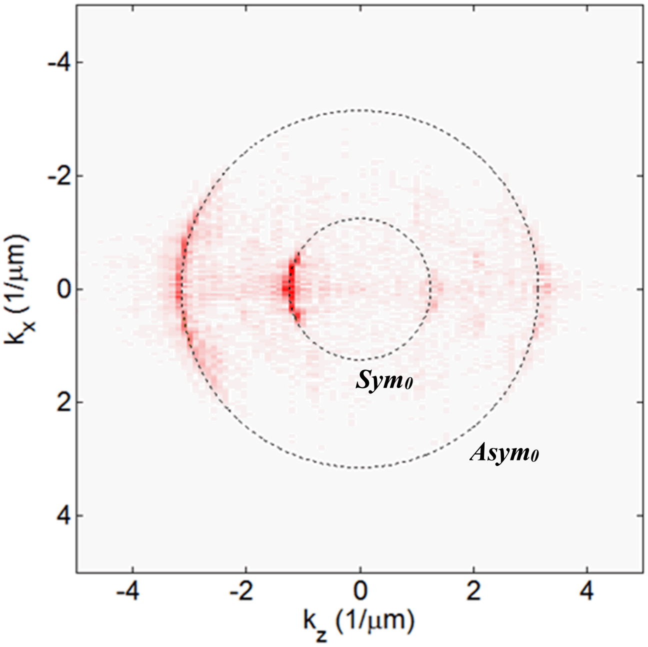

Figure 18. Fourier transform of measured out-of-plane displacement at the bottom-plane of the AlN membrane. Inner dashed ring corresponds to a k-vector radius of 1.25 $\mu m^{-1}$ (symmetric mode) and outer dashed ring corresponds to 3.15 $\mu m^{-1}$(anti-symmetric mode).

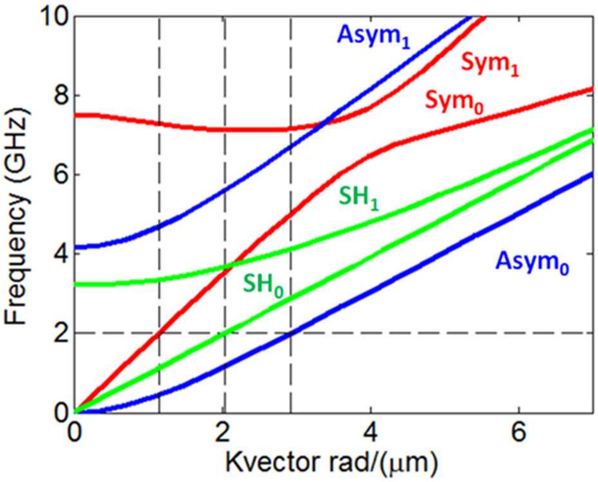

Figure 19. Dispersion relations for symmetric (blue) Lamb wave, anti-symmetric (red) Lamb waves and shear horizontal (green) waves for a 750nm AlN membrane. The bar indicates the modes at the excitation frequency.

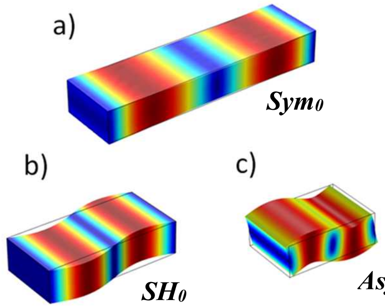

Figure 20. Mode profiles from the dispersion relations for the a) symmetric, b) shear horizontal and c) antisymmetric, at 2GHz.

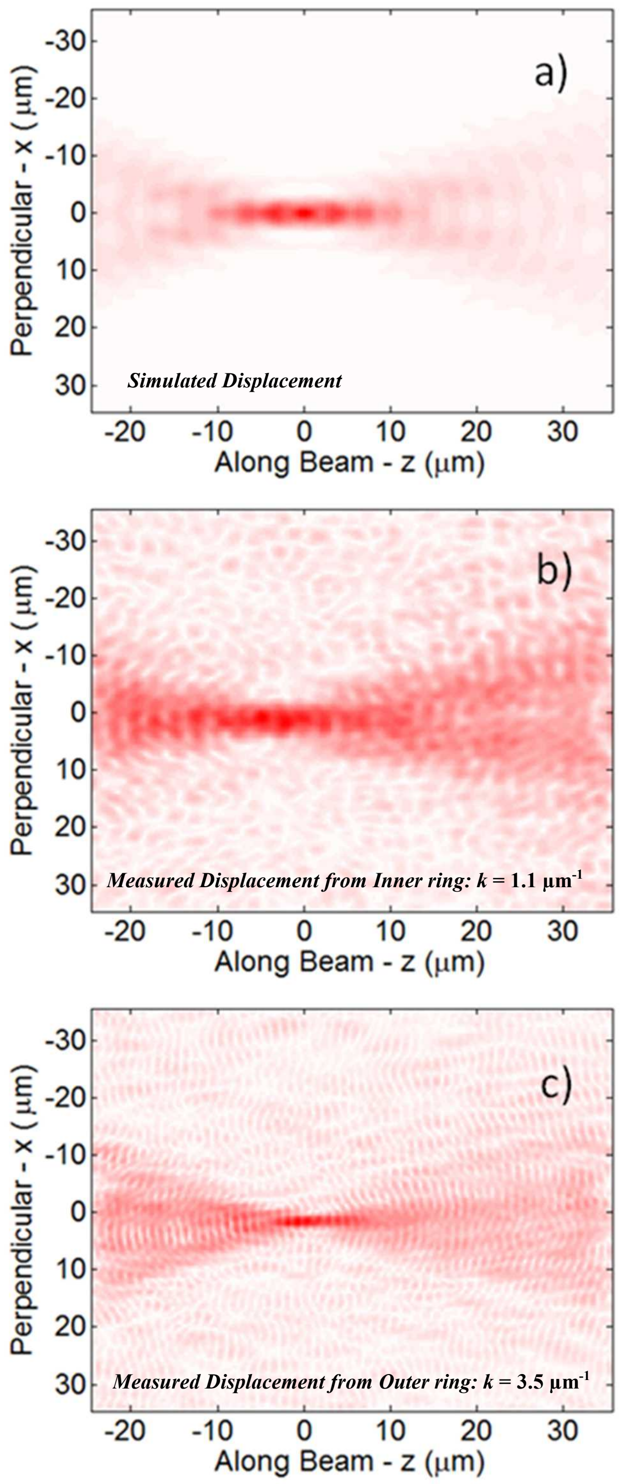

Figure 21. a) Field profile of vertical displacement at the bottom-plane of the AlN membrane from FEM simulation. b) Field profile corresponding to inner ring in k-space of the experimental data. c) Field profile corresponding to the outer ring.

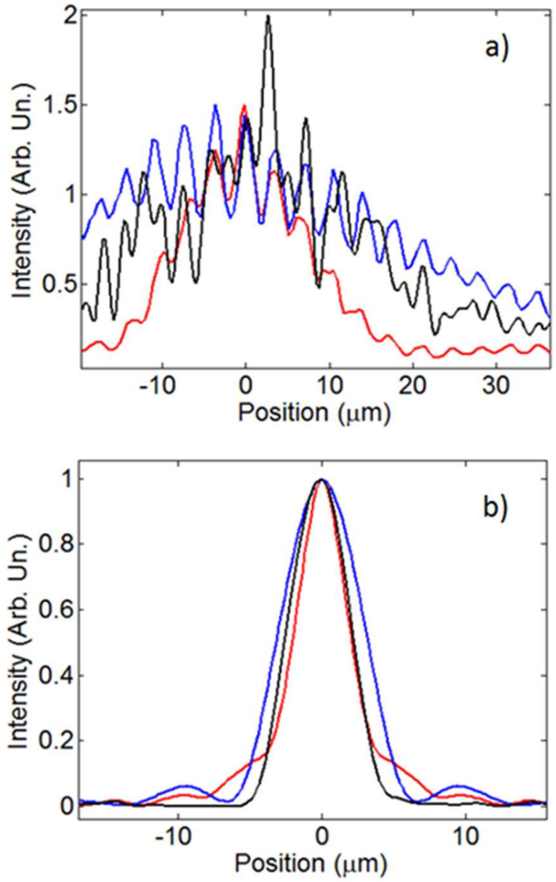

Figure 22. a) Intensity cross section of vertical displacement at the bottom-plane of AlN membrane along center of the propagation direction. Blue curve corresponds to FEM simulation with narrow transducer aperture ($\theta_D = .9$ rad). Red curve corresponds to simulated the wider aperture ($\theta_D = 1.5$). Black curve corresponds to experimental data. b) Corresponding intensity profile of displacement for cross section at focus position illustrating the beam waists.

angular dependence of the frequency amplitude along the inner ring in k-space which is shown in Fig. 23. As plotted in the figure, the curve for the experimental data is more localized than that predicted from the FEM model of transducer which were designed with an angular aperture of $\theta_D = 1.5$ rad. Additionally we have plotted the corresponding curve for an FEM simulation of a transducer with an angular aperture of $\theta_D = .9$ rad. As indicated by the agreement in the figure, the experimental data is better represented by a transducer with a narrower aperture. Additionally, the sectional plots in Fig. 22 show that the focused waist and Rayleigh range are better modeled with transducers having the narrower aperture.

This deviation of the measured displacement field profile from the predicted profile is worth addressing. Since the measured field distribution is better matched with a narrower aperture, the field amplitude beneath the transducers wings is less than that predicted by the local transducer width in equation 15. Local heating is one potential explanation for the observed reduction in transduction efficiency at these regions and observed narrowing of predicted spread in angle in k-space. As the transducers narrow toward the edge of the aperture range, the electrical resistance increases and correspondingly local resistive heating increases resulting in an impedance mismatch due to a temperature gradient and reduced excitation efficiency.

Additionally, we observe that coupling to the first order anti-asymmetric mode is larger than the theoretical prediction. FEM simulations indicate less than .3% coupling into this mode but these simulations don't account for all sources of asymmetry. Asymmetry due to local heating on the top plane, or mass loading are possible sources of asymmetry that result in enhanced coupling to the first asymmetric mode.

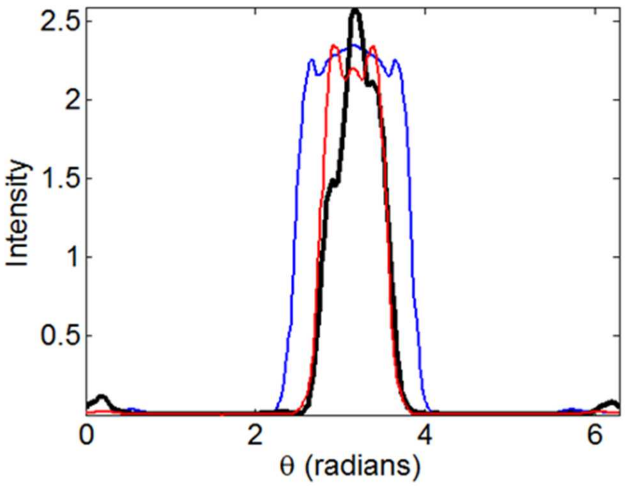

Figure 24. Angular dependence of Fourier amplitude along inner (black curve) of the experimental data. Angular dependence of Fourier amplitude from FEM simulation with transducer aperture, $\theta_{D,}$ set to 1.5 rad (blue curve) and .9 rad (red curve), illustrating the experimental data more closely matches fields generated with smaller apertures transducer.

## VII. DUAL-PORT DEVICES

As a final test of the Lamb beam transducers in this work, we experimentally evaluate their ability to focus energy in a device architecture by studying the inclusion of a hard-stop aperture in a send and receive configuration. The dual port devices considered here are comprised of identical send and receive focusing transducers, having the design studied in the previous sections, connected by a subwavelength acoustical waveguide serving as the aperture. The acoustical waveguide has a length set to match the acoustical wavelength, λ, and widths that vary from λ/2 to 10λ. Fig. 24 shows the fabricated devices for the cases of the narrowest and widest pinhole waveguides. Since λ=5µm for the devices here these correspond to widths of 2.5µm and 50 µm for the narrowest and widest waveguides respectively.

The transmission loss of a hard aperture can be determined by integrating the mode profile over the aperture window. Thus, for focused lamb modes in the Gaussian limit, equation (5) can be integrated to yield:

$$P_t/P_0 = \mathrm{erf}[D/(\sqrt{2}w(z))]; \qquad (22)$$

Where *erf()* is the error function, *D* is the aperture width, *z* is the distance from the focusing point, and $w(z)$, is the beam waist. In the devices considered here, the aperture is positioned at the focus, therefore, by setting $w(z) = w_0 = 2\lambda/\pi$ and evaluating the above equations for the devices in Fig. 24, we expect 3 dB of acoustic loss due to the hard aperture for the narrow aperture device (0.5λ-wide) and negligible acoustic loss for the wide aperture device (10λ-wide). The electrical characterization of these devices are shown in Fig. 25. The narrow-aperture device only incurs 0.5 dB of additional loss in reflection and ~3dB additional loss in transmission relative to the wide-aperture device, thus confirming that the acoustical power is indeed focused through a narrow hard aperture.

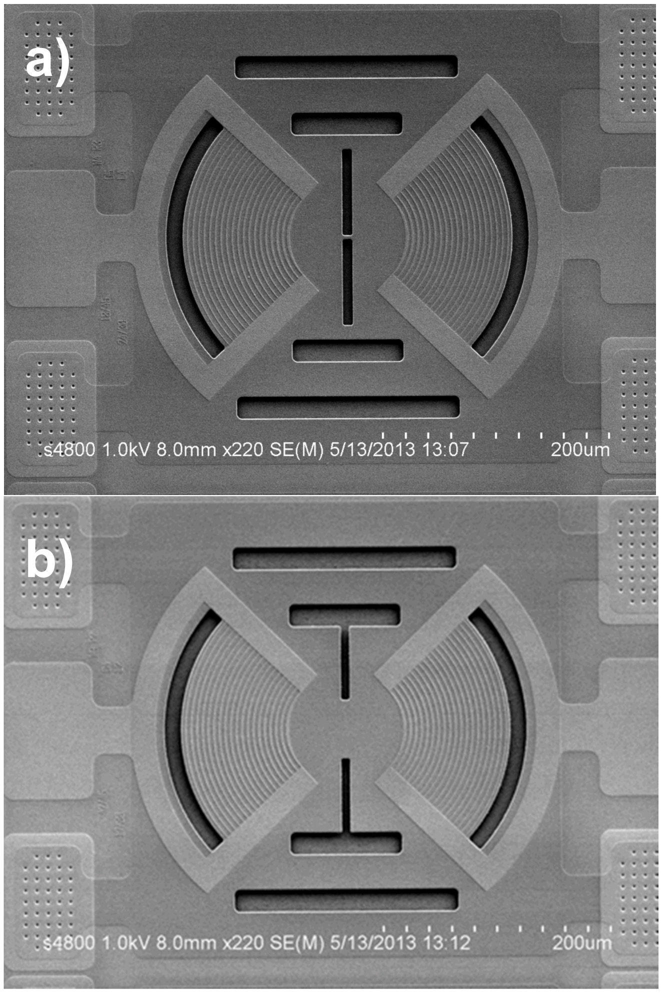

Figure 23. Fabricated dual-port devices, one with a 0.5λ waveguide (2.5µm wide) (a) and the other with a 10λ waveguide (b), which is essentially a wide-open aperture.

Additionally, we performed confocal imaging and k-space analysis on the narrow-aperture devices. The corresponding displacement field image measured with our confocal imaging setup is shown in Fig. 26 and illustrates the focusing and coupling action of the designed transducers. The k-space composition of the mode, is shown and forms concentric rings. As with the single port devices, both the symmetric and anti-symmetric modes are excited. The inner most ring and outer most ring corresponds corresponding to symmetric and anti-symmetric modes respectively have k-vector radii of 1.25 $\mu m^{-1}$. and 3.15 $\mu m^{-1}$. For the two-port case, however, there is strong

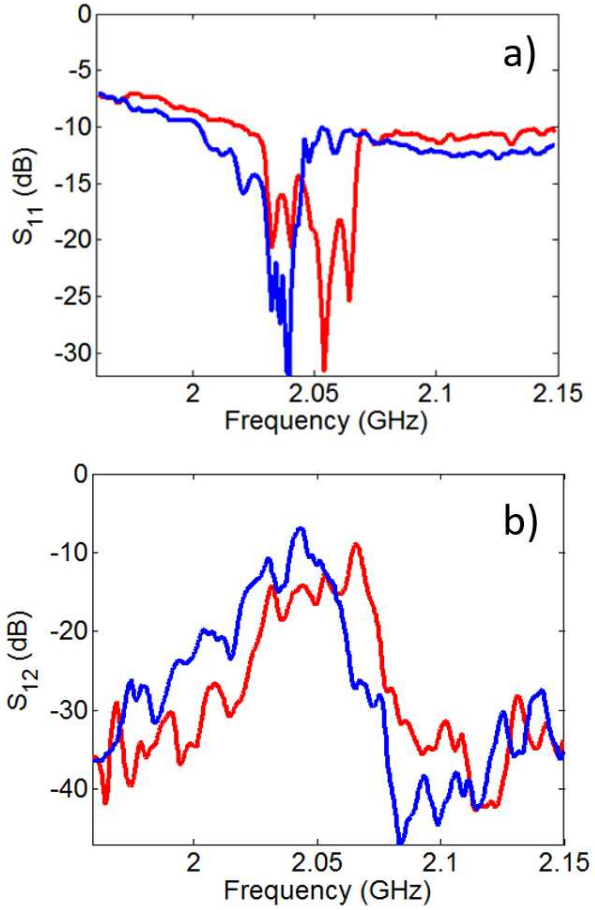

Figure 26. Electrical characterization of a 0.5λ (red) and 10λ (blue) wide waveguide two-port devices, showing a negligible increase in insertion loss for the 0.5λ device.

amplitude at both positive and negative k on a ring, indicating the presence of both forward and backward going waves of nearly equal amplitude. This is expected given that the structure essentially forms a linear confocal cavity, given the end reflectors at the send and receive ports, with a central aperture.

The middle ring in the k-space diagram in Fig. 26, however, identifies an additional mode involved in the interaction; a mode not involved in the single port devices. Its value of k-vector radii of 2 $\mu m^{-1}$ indicates that the mode is a shear horizontal mode (SH) as determined from the dispersion diagram in Figure 19 19. Although the transducers themselves are not able to excite shear horizontal modes, the interaction with the waveguide causes coupling between the symmetric, antisymmetric, and shear horizontal modes which results in a weak mode mixing such that the resulting quasi-shear mode has a small but detectable out of plane component.

As was done in the previous section, the concentric rings can each be filtered out individually to visualize the beam profile associated with the mode class and the results are reported in Fig. 27. Fig. 27(a) shows that the symmetric mode contribution to the image is smooth and continuous through the waveguide confirming that on resonance the symmetric mode is focused

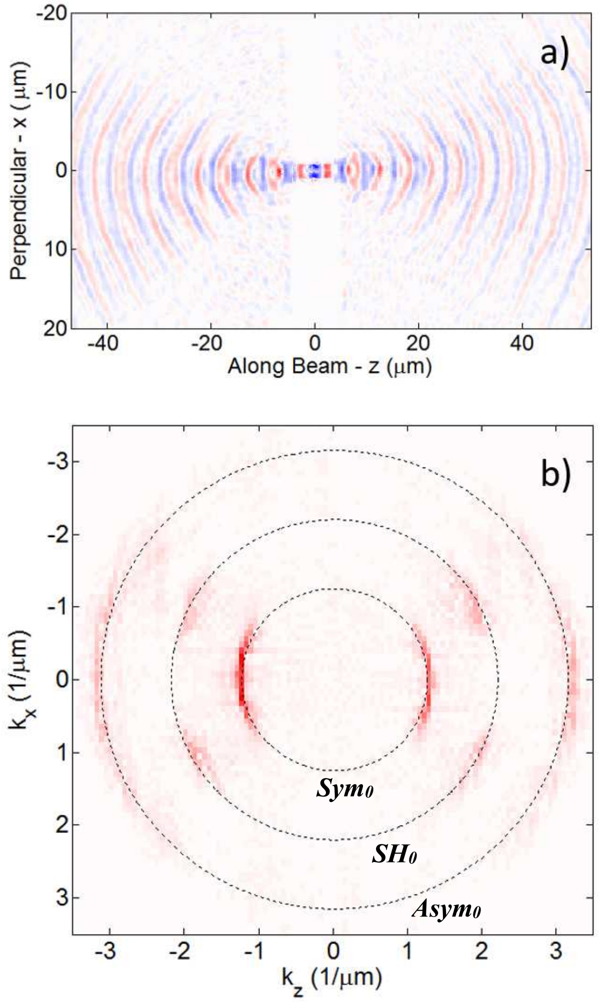

Figure 25. a) Measured optical image displacement field (real part) of dual port device with a 0.5λ waveguide (2.5μm wide). b) Fourier transform (k-space) of (a). Inner dashing ring corresponds to 1.25$\mu m^{-1}$, the middle ring corresponds to 2 $\mu m^{-1}$, and the outer ring corresponds to 3.15 $\mu m^{-1}$ corresponding to beams formed with symmetric, shear horizontal respectively and anti-symmetric respectively.

unobstructed through the hard aperture. The prominent fringing pattern is due to the backward going wave, and indicates that a single wavelength contained in the waveguide. Fig. 27(b) shows the antisymmetric mode contribution. The length of the waveguide while resonant for the symmetric mode is not resonant for the anti-symmetric mode, and therefore power is not continuous through the waveguide. A small portion of the incident wave scatters at the waveguide input into the asymmetric mode which is contained in the side cavity formed between the send back-reflector waveguide input. The effect similarly happens with the backward going wave at the waveguide output resulting in a small amount of energy leaking into an antisymmetric mode being contained in the side cavity formed by the waveguide output and the receiver back-reflector. Finally, Fig. 27(c) shows the beam contribution from the SH modes. As with the antisymmetric mode, the waveguide length is not resonant with the SH k-vector resulting in low field amplitude at the center of the waveguide and quasi-SH modes

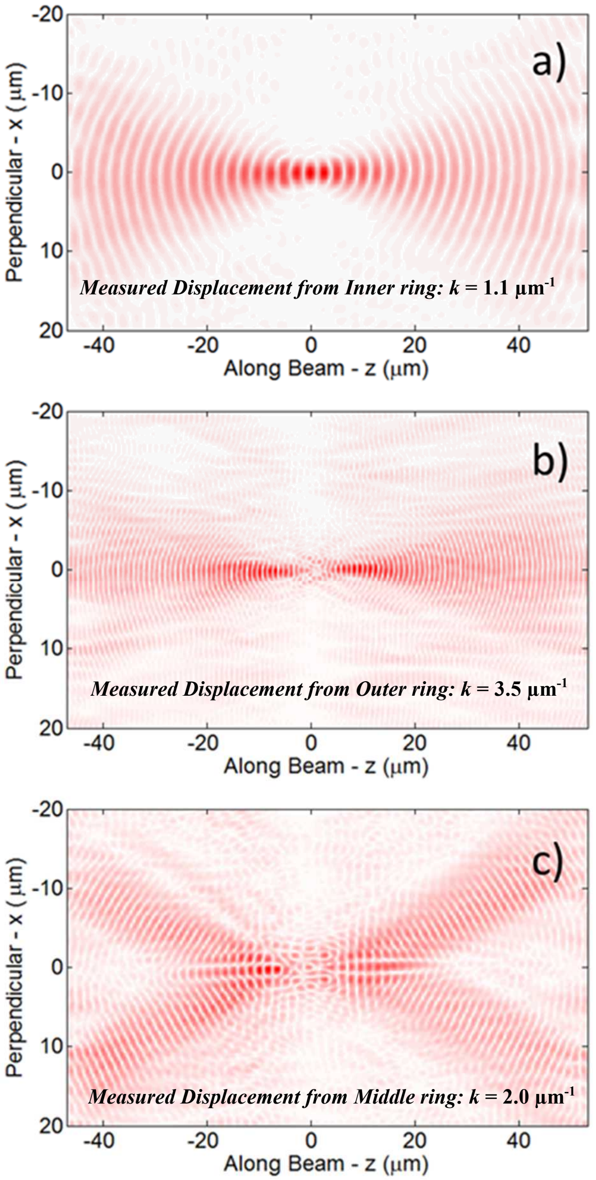

Figure 27. Filtered profiles of the inner (a), outer (b) and middle ring (c) from k-space in Fig. 24 corresponding to beams formed with symmetric, anti-symmetric and shear horizontal respectively.

developing in the side cavities. Interestingly the excited SH mode is not the lowest order cavity mode but rather a higher order exhibiting a cross pattern. This cavity mode corresponds to aperture-limited Bessel beams in optics[21].

As was mentioned for the single port device, the measured confocal images represent vertical displacement at the bottom plane only, although the majority of the displacement is radial at the mid plane. Thus, we would need to normalize the relative energy along the contours of the symmetric, antisymmetric and shear horizontal modes to calculate the forward going power of the mode in order to quantify the modal efficiency of the transducer. Hybridization of the modes for the resonant device considered complicates this procedure. However, the effective coupling constant of the receive transducer effectively serves as a notch filter for the targeted symmetric mode. Therefor the electrical measurements indicate that the majority of displacement energy is in the symmetric mode. And the analysis on the confocal imaging data illustrates the utility of the k-space representation to understand the interaction of modes of differing k-vector for the given operating frequency.

## VIII. Discussion and Conclusions

In this work, we provided a comprehensive study of the design, modeling, fabrication, and experimental verification of transducers that produce focused Lamb wave beams in thin-film aluminum nitride membranes. In particular, we developed a theoretical description of focused Lamb beams in thin films and presented a Fourier domain design methodology that we employed to design and fabricated both single and dual-port devices in a 750nm AlN membrane. The single-port devices enabled demonstration of diffraction limited focusing, which we confirmed through confocal imaging. We showed that the transducers in this work achieve a diffraction limited focused spot size of 5µm at 2GHz where the wavelength of the symmetric mode is 5.3 µm. Modal analysis in k-space shows that we achieve more than 85% efficiency into the desired focused beam formed with the symmetric mode. Additionally, we demonstrated a functional two-port device utilizing focusing transducers. Focusing enabled coupling energy through a wavelength scale aperture with minimal relative insertion loss. Analysis of the confocal image in the Fourier domain allows us to understand the roles of the symmetric, antisymmetric and shear horizontal beams. Although the overall insertion loss of our two-port devices was of order 10 dB, much of this loss is completely avoidable with moderate changes in busing and fabrication, and we are already taking steps to design devices with much lower total insertion loss.

The theory, analysis, and results presented here with one and two port devices, together, demonstrate the ability to efficiently produce focused Lamb beams directly from carefully designed curved ITDS and to excite wavelength-scale structures. We believe this result holds great promise for the technological utilization of microwave electromechanical devices that incorporate wavelength scale structures, such as phononic crystal waveguides and cavities. We are confident that focused IDTs will find boarder use as the field of wavelength scale phononic devices matures.

Sandia National Laboratories is a multi-mission laboratory managed and operated by NTESS of Sandia, LLC., a wholly owned subsidiary of Honeywell International, Inc., for the U.S. Department of Energy's National Nuclear Security Administration under contract DE-NA0003525. This work was supported by the Laboratory Directed Research and Development Program and Truman Fellowship. The views, opinions, and/or findings expressed are those of the author(s) and should not be interpreted as representing the official views r policies of the Department of Defense or the U.S. Government. The authors acknowledge fabrication support by the Sandia MESA-Fab operations team and test and measurement support by J. A. Trevino, J. K. Douglas, and P.

Stanfield.

[1] L. Wang, S. M. Chen, X. Ning, Z. Chen, J. T. Liu, and J. Y. Zhang, “Embedded nanotransducer for ultrahigh-frequency SAW utilizing AlN/diamond layered structure,” in *2017 Joint IEEE International Symposium on the Applications of Ferroelectric (ISAF)/International Workshop on Acoustic Transduction Materials and Devices (IWATMD)/Piezoresponse Force Microscopy (PFM)*, 2017, pp. 106–109.

[2] J. J. Chen, F. Zeng, D. M. Li, J. B. Niu, and F. Pan, “Deposition of high-quality zinc oxide thin films on diamond substrates for high-frequency surface acoustic wave filter applications,” *Thin Solid Films*, vol. 485, no. 1, pp. 257–261, Aug. 2005.

[3] K. M. Lakin, G. R. Kline, and K. T. McCarron, “High-Q microwave acoustic resonators and filters,” *IEEE Trans. Microw. Theory Tech.*, vol. 41, no. 12, pp. 2139–2146, Dec. 1993.

[4] S. Mohammadi, A. A. Eftekhar, W. D. Hunt, and A. Adibi, “High-Q micromechanical resonators in a two-dimensional phononic crystal slab,” *Appl. Phys. Lett.*, vol. 94, no. 5, p. 051906, Feb. 2009.

[5] P. H. Otsuka *et al.*, “Broadband evolution of phononic-crystal-waveguide eigenstates in real- and k-spaces,” *Sci. Rep.*, vol. 3, Nov. 2013.

[6] D. Hatanaka, I. Mahboob, K. Onomitsu, and H. Yamaguchi, “Phonon waveguides for electromechanical circuits,” *Nat. Nanotechnol.*, vol. 9, no. 7, pp. 520–524, Jul. 2014.

[7] S. Mohammadi and A. Adibi, “Waveguide-Based Phononic Crystal Micro/Nanomechanical High- Resonators,” *J. Microelectromechanical Syst.*, vol. 21, no. 2, pp. 379–384, Apr. 2012.

[8] M. Eichenfield, J. Chan, R. M. Camacho, K. J. Vahala, and O. Painter, “Optomechanical crystals,” *Nature*, vol. 462, no. 7269, pp. 78–82, Nov. 2009.

[9] J. Chan *et al.*, “Laser cooling of a nanomechanical oscillator into its quantum ground state,” *Nature*, vol. 478, no. 7367, pp. 89–92, Oct. 2011.

[10] H. Shin *et al.*, “Tailorable stimulated Brillouin scattering in nanoscale silicon waveguides,” *Nat. Commun.*, vol. 4, Jun. 2013.

[11] H. Shin, J. A. Cox, R. Jarecki, A. Starbuck, Z. Wang, and P. T. Rakich, “Control of coherent information via on-chip photonic–phononic emitter–receivers,” *Nat. Commun.*, vol. 6, p. 6427, Mar. 2015.

[12] P. J. Shull, *Nondestructive Evaluation: Theory, Techniques, and Applications*. CRC Press, 2016.

[13] D. Royer and E. Dieulesaint, *Elastic Waves in Solids II: Generation, Acousto-optic Interaction, Applications*. Springer Science & Business Media, 2000.

[14] R. H. Olsson *et al.*, “Ultra high frequency (UHF) phononic crystal devices operating in mobile communication bands,” in *Ultrasonics Symposium (IUS), 2009 IEEE International*, 2009, pp. 1150–1153.

[15] M.-H. Lu, L. Feng, and Y.-F. Chen, “Phononic crystals and acoustic metamaterials,” *Mater. Today*, vol. 12, no. 12, pp. 34–42, Dec. 2009.

[16] Kuypers, “Green’s function analysis of Lamb wave resonators.”

[17] J. H. Kuypers, D. A. Eisele, and L. M. Reindl, “The k-model - green’s function based analysis of surface acoustic wave devices,” in *IEEE Ultrasonics Symposium, 2005.*, 2005, vol. 3, pp. 1550–1555.

[18] S. G. Joshi and Y. Jin, “Propagation of ultrasonic Lamb waves in piezoelectric plates,” *J. Appl. Phys.*, vol. 70, no. 8, pp. 4113–4120, Oct. 1991.

[19] V. Yantchev and I. Katardjiev, “Quasistatic transduction of the fundamental symmetric Lamb mode in longitudinal wave transducers,” *Appl. Phys. Lett.*, vol. 88, no. 21, p. 214101, May 2006.

[20] P. Wilcox, R. Monkhouse, M. Lowe, and P. Cawley, “The Use of Huygens’ Principle to Model the Acoustic Field from Interdigital Lamb Wave Transducers,” in *Review of Progress in Quantitative Nondestructive Evaluation*, D. O. Thompson and D. E. Chimenti, Eds. Springer US, 1998, pp. 915–922.

[21] H. A. Haus, *Waves and Fields in Optoelectronics*. Englewood Cliffs, NJ: Prentice-Hall, 1984.

[22] D. G. Duffy, *Green’s Functions with Applications*. CRC Press, 2001.

[23] Y. A. Kravtsov and P. Berczynski, “Description of the 2D Gaussian beam diffraction in a free space in frame of eikonal-based complex geometric optics,” *Wave Motion*, vol. 40, no. 1, pp. 23–27, Jun. 2004.

[24] B. A. Auld, *Acoustic Fields and Waves in Solids*. Krieger Publishing Company, 1990.

[25] G. Santoni, “Fundamental Studies in the lamb-wave interaction between piezoelectric waffer active sensor and host structure during structural health monitoring,” *Thesis*, 1999.

[26] “A treatise on the theory of Bessel functions.” [Online]. Available: https://archive.org/stream/treatiseontheory00watsuoft#page/390/mode/2up. [Accessed: 11-Jul-2014].

[27] F. W. J. Olver, *NIST Handbook of Mathematical Functions Hardback and CD-ROM*. Cambridge University Press, 2010.

[28] S. G. Joshi and Y. Jin, “Excitation of ultrasonic Lamb waves in piezoelectric plates,” *J. Appl. Phys.*, vol. 69, no. 12, pp. 8018–8024, Jun. 1991.

[29] A. D. Poularikas, *Handbook of Formulas and Tables for Signal Processing*. CRC Press, 1998.

[30] A. V. Oppenheim, *Signals and Systems*. Prentice Hall, 1997.

[31] G. Piazza, V. Felmetsger, P. Muralt, R. H. Olsson III, and R. Ruby, “Piezoelectric aluminum nitride thin films for microelectromechanical systems,” *MRS Bull.*, vol. 37, no. 11, pp. 1051–1061, Nov. 2012.

[32] G. G. Fattinger and P. T. Tikka, “Modified Mach–Zender laser interferometer for probing bulk acoustic waves,” *Appl. Phys. Lett.*, vol. 79, no. 3, pp. 290–292, Jul. 2001.

[33] J. V. Knuuttila, P. T. Tikka, and M. M. Salomaa, “Scanning Michelson interferometer for imaging surface acoustic wave fields,” *Opt. Lett.*, vol. 25, no. 9, pp. 613–615, May 2000.